JMEPEG (2022) 31:6420–6434
https://doi.org/10.1007/s11665-022-06707-6

1059-9495/$19.00

TECHNICAL ARTICLE

Influence of Salt-Bath Nitrocarburizing on the Electrochemical Corrosion Properties of Stainless Steels and Nickel-Based Alloys in 3.5-wt.% Sodium Chloride Solution

Virendra Singh and Manuel Marya

Submitted: 27 September 2021 / Revised: 21 December 2021 / Accepted: 8 February 2022 / Published online: 23 February 2022

Stainless steels and nickel-based alloys, despite adequate corrosion resistance for general oilfield services, are restricted in abrasive and fretting wear by their surface hardness. Nitrocarburizing is well known to cause surface hardening, but its effect on corrosion is still not well established on high-chromium iron and nickel-based alloys. Salt-bath nitrocarburizing has been applied on five stainless steels (UNS S41000, UNS S41425, UNS S17400, UNS S30400, and UNS S31600) and four nickel-based alloys (UNS N09925, UNS N09935, UNS N07718, and UNS N07716) to explore the effects of alloy compositions on nitrocarburizing compounds, case depths, and corrosion behaviors in a light 3.5 wt.% sodium chloride brine. For all selected alloys, the nitrocarburized surfaces were mainly characterized by optical and scanning electron microscopy and x-ray diffraction. In addition to pit quantification measurements, corrosion resistance was evaluated by cyclic potentiodynamic polarization testing at ambient temperature on both un-nitrocarburized and nitrocarburized alloys, the latter simultaneously processed in a single molten salt bath. Compared to the nickel-based alloys, the nitrocarburized stainless steels possess thicker and harder compound layers of chromium nitrides, with an iron (III) oxide layer on top. Potentiodynamic polarization tests further indicate that nitrocarburizing increases the corrosion resistance of stainless steels at least temporarily. The nickel-based alloys, characterized by thinner nitride layers, were all observed to lose some corrosion resistance, yet remained comparable in pitting resistance than the un-nitrocarburized stainless steels with a minimum PREN of approximately 20. The nitrocarburized nickel-based alloys were consistently found to be free of both iron (III) oxide at the surface and nitrogen enrichment below the compound layer. Carbon was found to cluster below the nitride-rich compound layer, with its contributions in need of further investigations.

Keywords corrosion, cyclic potentiodynamic polarization, nickel-based alloys, nitride compound layer, passivity, pitting, salt-bath nitrocarburizing, stainless steels

1. Introduction

In hydrocarbon production, carbon sequestration, and subterranean geothermal environments, stainless steels and nickel-based alloys are often encountered as critical load-bearing alloys because of attractive combinations of mechanical properties and corrosion resistance. The stainless steels, explicitly ferrous alloys with more than about 12.5 wt.% chromium (Cr) that have been further modified with 2-5 wt.% nickel (Ni) and over 1 wt.% molybdenum (Mo), are generally deployed in non-corrosive and mildly corrosive environments. To develop useful mechanical properties, these alloys are all delivered in quenched and tempered conditions with typical minimum yield strengths of 552-758 MPa (80-110 ksi). For harsher environments, the precipitation-hardened nickel-based alloys are selected as a normal upgrade to the stainless steels and advantageously offer minimum yield strengths of 758-960 MPa (110-140 ksi). These nickel-based alloys, specifically Ni-Fe-Cr-Mo alloys, possess superior combinations of mechanical strength and toughness. Additionally, they have been successfully used for decades in environments with elevated sour gas (H_2S), carbon dioxide (CO_2), and a whole range of brines (Ref 1). For subterranean equipment, nickel-based alloys are preferred over stainless steels because of their greater weight-loss corrosion resistance, improved localized corrosion resistance, as well as their established track records against chloride stress and sulfide stress corrosion cracking, as documented and specified by industry standards such as NACE MR0175/ISO 15156 (Ref 2). In order of increasing nickel and molybdenum contents, the typical nickel-based alloys include Alloy 925 (UNS N07925), Alloy 718 (UNS N07718), and Alloy 625^{Plus} (UNS N07716). Despite a relatively limited consumption, Alloy 935 (UNS N09935), a relatively newer alloy introduced in the mid-2000s to fulfill a performance–cost gap market demand, has also been included in this investigation to establish its nitrocarburizing response and its impact on this alloy corrosion resistance.

Virendra Singh and **Manuel Marya**, Schlumberger Technology Corporation, 14910 airlines road, Rosharon, Texas 77583. Contact e-mail: VSingh10@slb.com.

The equipment fabricated from these corrosion-resistant alloys is almost always exposed to some forms of abrasive, adhesive, fatigue, and/or erosive wear, leading to surface damages. To specifically protect critical surfaces and prolong equipment's useful life in the fields, a variety of engineering coatings and surface treatments have become established across applications. These include electroless plating and electroplating (e.g., nickel, cobalt) as well as thermal diffusion treatments, e.g., nitriding, nitrocarburizing (where nitrogen is dominant over carbon), carbonitriding (where carbon is dominant over nitrogen), and boronizing or boriding (Ref 3). In addition to wear resistance, other major technical advantages of these surface treatments include a more predictable frictional behavior in dynamic applications, the suppression of galling and fretting, all without any perceptible dimensional changes and noticeable alterations in minimum specified mechanical properties (Ref 4, 5). Surface treatments by thermal diffusion produce a surface hardening response that stems from the interstitial diffusion of nitrogen, carbon, or boron, followed by the formation of stable ceramic-like compounds such as nitrides, carbides, and borides (Ref 6-8). While interstitial atomic diffusion leads to only a moderate level of surface hardening, the formation of compounds contributes greatly to elevated hardness values (Ref 9).

For the typical stainless steels, nitrocarburizing causes nitrogen and/or carbon atoms to penetrate the surface and form hard compound layers, predominantly comprised of chromium (I) nitride (CrN), but also at least two stochiometric iron nitrides, $Fe_2(N,C)$ and $Fe_{3-4}N$ (Ref 10). The formation of nitrides increases the surface hardness between 950 and 1600 HVN, resulting in improved abrasive wear as well as fatigue resistance under normal conditions (Ref 11). Depending upon alloy chemical composition and nitrocarburizing process, a process cycle can vary in time from 2 to 50 h (Ref 12). Based on previous investigations and some accumulated experience in nitrocarburizing industrial components, the nitride compound thickness varies between approximately 2-75 μm depending upon nitrocarburizing time, temperature, molten salt chemistry, and alloy composition (Ref 3). To develop the proper and effective nitrocarburized surfaces, the nickel alloys always require considerably longer processing cycles, as high as 40 hours compared to the common two-hour cycle for carbon, low-alloy steels, and stainless steels (Ref 13). The nickel-based alloys, being less conducive to nitrocarburizing response, tend to be more suitable to plasma nitriding (ion nitriding), a characteristic that translates into economic disadvantages, among others. A number of investigations can be found in the technical literature on plasma nitriding, nitrocarburizing, low-temperature plasma nitriding and nitrocarburizing of stainless steels, and their effects on wear and abrasion characteristics (Ref 14-16), whereas little is comparatively available for nickel-based alloys such as Alloys 718 (Ref 16) and 625 (Ref 17, 18). The literature more specifically addressing the corrosion of nitrocarburized stainless steels is also limited (Ref 19-22). The nitrocarburizing of nickel alloys is not widespread across industries and remains restricted by the general nitridability of these alloys and their inability to meet stringent wear application requirements (Ref 23, 24). On the environmental compatibility of nitrocarburizing, Hongyi li et al. have demonstrated improvements in corrosion resistance on Alloy 304 in a sour gas environment and largely explained it by oxide and the nitrogen-rich layers that apparently reduce hydrogen permeation (Ref 21). Overall, it is of general industrial interest to clarify the impact of nitrocarburizing on the corrosion of common subterranean alloys, not only for the well-established hydrocarbon exploration and production-proven applications but also the newer carbon sequestration and geothermal applications. For all these environments where the end applications may demand surface treatments, preferably simple and economical, the possibility of accelerated general corrosion or localized corrosion by pitting or crevice corrosion is concerning and provides a strong driver for this investigation.

For this investigation, two quenched and tempered martensitic stainless steels, Alloy 13Cr (UNS41000) and Alloy S13Cr (UNS41425), and precipitation-hardened stainless steel, 17-4PH (UNS17400 in HH1150 condition), were selected and complemented by two standard non-heat-treatable austenitic stainless steels, Alloys 304 (UNS30400) and 316 (UNS31600). Four precipitation-hardened nickel-based alloys, namely Alloys 925 (UNS N09925), 935 (UNS N09935), 718 (UNS N07718), and 625^{Plus} (UNS N07716), were also chosen. As a whole, these alloys present considerable differences: nickel (Ni) contents range from 32 to 56 wt.%, chromium (Cr) from 20 to 22 wt.%, while molybdenum (Mo) reaches up to 6 wt.% for Alloy 625^{Plus}. For pragmatic considerations, salt-bath nitrocarburizing was preferred over the other nitriding processes because also non-line-of-sight, relatively low temperature, and quite routinely applied to existing field equipment. Following salt-bath nitrocarburizing, microstructural characterization and electrochemical corrosion testing were conducted to determine relationships between alloy composition, nitrocarburizing response, general and pitting corrosion, both evaluated by cyclic potentiodynamic testing. Practically, this investigation proposes to shed some light on the effects of nitrocarburizing on the corrosion of two alloy families represented by their broad compositional ranges. Due to the selected testing methodology, the authors expect the findings of this investigation to primarily apply to short-term exposure to light brines, including seawater, and implicitly generalizing or extrapolating the results of this investigation to other conditions shall be therefore conducted with cautions.

2. Experimental Procedure

In this investigation, five stainless steels and four nickel-based alloys were acquired as solid round bars in finished heat-treated conditions. Alloys 13Cr, S13Cr, and 17-4PH were provided in their quenched and tempered, or hardened condition, whereas Alloys 304 and 316 were received in annealed, thus in their softest condition. Alloys 925, 935, 718, and 625^{Plus} were all received in their normal aged or precipitation-hardened condition according to API Spec 6ACRA (Ref 25). For the electrochemical testing, rectangular test samples (50mm × 50mm × 12.5mm) were machined from solid bar stocks, ground, and polished to a 600-grit finish. The chemical compositions and mechanical properties of all alloys of this investigation are disclosed in Table 1, 2. Both stainless steels and nickel-based alloys are listed in order of increasing chromium (Cr) and/or molybdenum (Mo) contents. To capture the combined contribution of these elements, the Pitting Resistance Equivalent Number (PREN= %Cr + 3.3%Mo + 19.4%N) is also included in the table to later attempt simple and valuable correlations with the corrosion results (Ref 26). Even though indiscriminately applying a PREN to different

Table 1 Chemical compositions (in wt.%) of the stainless steels and calculated PREN

	C	Mn	Mo	Si	Cu	Ni	Cr	Nb	N	V	Fe	PREN
13Cr	0.125	0.52	0.04	0.39	0.072	0.45	13.12	0.03	0.06	0.04	85	14
S13Cr	0.015	0.34	1.95	0.2	0.04	5.37	12.12	…	0.012	0.16	79.8	18.7
17-4PH	0.04	0.6	0.2	0.3	3.19	4.2	15.8	0.24	…	…	75.4	16.5
304	0.07	1.5	…	0.75	…	9.5	18.5	…	0.1	…	69.65	20
316	0.08	1.4	2.5	0.90	…	11	17.5	…	…	…	66.3	25

Table 2 Chemical compositions (in wt.%) of the nickel-based alloys and calculated PREN

	C	Mn	Mo	Si	Cu	Ni	Cr	Al	Ti	Nb+Ta	Co	Fe	PREN
718	0.015	0.06	2.9	0.07	0.09	53.5	18.5	0.52	1.0	4.96	0.145	18.3	28
925	0.02	0.53	2.92	0.12	1.72	44.06	20.70	0.23	2.14	0.44	…	27	30
935	0.016	0.4	3.7	0.04	1.43	36.2	20.1	0.23	2.10	0.3	0.03	35.44	32.3
625^{Plus}	0.015	0.1	8.05	0.1	0.22	61.49	20.92	0.22	1.18	3.31	…	4.4	47.5

alloy families is arguable, this investigation indirectly addresses the effect of PREN from a minimum value of 14 for Alloy 13Cr to 47.5 for Alloy 625^{Plus}. The literature suggests that this range in PREN translates into critical pitting temperature between ~5 and ~65 °C as per ASTM standards G48 and G150 (Ref 27, 28). Implicitly, the authors anticipate that PREN could be a simple and practical indicator for discussing the corrosion of the various alloys with and without nitrocarburizing. Given the broad range of critical pitting temperatures, the formation of crevices may be normally expected over a fairly short time, and therefore, a special procedure was developed to also eliminate any unintentional crevice corrosion, as later described.

For the salt-bath nitrocarburizing treatment, polished square coupons of each material (25mm × 25mm) were subjected to proprietary liquid bath at 580 °C (990°F) for 120 minutes. The selected industrial molten salt chemistry is known to reliably produce nitrides primarily. This paper will emphasize the contributions of nitrogen, keeping in mind that carbon is also present in the molten salt. The nitrocarburizing process in use consists of three standard consecutive stages common to all alloys: (1) degreasing, (2) nitrocarburizing at 580 °C for about 120 minutes, and (3) a post-oxidation treatment at 425 °C for about 20 minutes. The post-oxidation has similarities with black oxide treatments, a major intent being to improve atmospheric corrosion resistance supplementarily. All nitrocarburized samples were tested only after a subsequent cleaning cycle with acetone and finally deionized water. Following oxidation of the test samples, none of the test samples were further polished out of concerns for altering their surfaces, particularly reducing the overall thickness of the hard compounds (Ref 8). As a result, the nitrocarburized surfaces were not as smooth as were initially conceived for detailed microstructural examinations, a limitation that made sample preparation prior to nitrocarburizing more important.

All test samples, un-nitrocarburized and nitrocarburized, were first metallurgically characterized. Then, x-ray diffraction was applied to identify each alloy metallurgical phase before and after nitrocarburizing. The x-ray diffractometer was set at 40 kV and 30 mA with a CuKα radiation target (λ~1.54 Å) and scanned all angles between 20 and 80 degrees at a rate of a degree per minute. The test samples were also cross-sectioned and prepared for standard metallographic examinations to estimate the hardening caused by the molten salt bath. Cross section microstructures were analyzed by optical microscopy using a Keyence VHX2000 (Japan) microscope, primarily to estimate compound layer thickness. Complementarily, Vickers microhardness measurements under 25g and 100g were conducted with a calibrated Future Tech. FM-7 microindenter (Japan) to further measure the hardening that develops below the compound layers. Throughout this investigation, the nitrocarburized test samples were consistently tested against their un-nitrocarburized alloy references. When applicable, laser confocal microscopy (Keyence VK-X1000), scanning electron microscopy (Carl Zeiss Ultra 55 SEM, Dresden, Germany), wavelength-dispersive spectroscopy (CAMECA SXFive), and image analysis (ImageJ software) were applied to quantify pit size and density and relates these to the various characteristics of nitrocarburized alloys.

To evaluate and compare the corrosion of the various alloys in both nitrocarburized and un-nitrocarburized conditions, cyclic potentiodynamic polarization testing was performed as per ASTM G61 (Ref 29). Measurements were completed at room temperature (23°C) using an aerated 3.5 wt.% sodium chloride deionized aqueous solution. Before initiating the cyclic polarization scans, all samples were pre-immersed a full hour to identify their open-circuit potential (OCP). The polarization tests were all completed with a Gamry ™ standard three-electrode system in a 1.25L flexible cell. The working electrode offered an exposed area of 2.5 cm^2, totally compatible with the test sample dimensions. For testing, the samples were mounted outside a PTFE holder cell, and with their working surface facing up. At the contact surface between a sample and cell, a small volume of deionized water was continuously circulated as a mean to prevent the formation of circumferential crevices, a situation that would otherwise invalidate any test and impose an additional repeat. The test samples were separated from the cell port using a filter paper ring. The cell consisted of a pair of graphite counter rods acting as a single electrode, a saturated calomel electrode (SCE) serving as a reference electrode, and a sample representing the working electrode. All tests were conducted with a constant scan rate of 0.2mV/sec, initiated at -200mV vs. the open-circuit potential (OCP), and continuing up

to 700 mV for stainless steels alloys, up to 1400 mV for the nickel-based alloys, and then reversed in the negative direction when either the current density exceeded five mA/cm^2 or the potential reach to the initial set peak values. The reverse scan was stopped at the initial OCP measured value. After completing the electrochemical scans, most test samples were inspected for signs of pitting using the laser confocal microscope.

3. Results and Discussion

3.1 Compound Layer Thickness Measurements

As the first general observation, the salt-bath nitrocarburizing treatment caused a homogeneously uniform darkening of all samples, indicating thermochemical responses toward the molten salt bath. The cross section microstructures of all nitrocarburized stainless steels and nickel-based alloys are presented in Fig. 1, followed by the microhardness profiles and exemplary compositional analyses in Fig. 2. Even without chemical etching, the cross section micrographs clearly reveal light/dark gray nitrocarburized layers at the alloy surfaces, all characterized by average thickness values that vary with alloy composition. This characteristic layer at the surface, most referred to in the literature as the compound layer, is shown in Fig. 1 for all the alloys and is found to correspond to the locations of maximum microhardness, as captured by Fig. 2. For the stainless steels, Fig. 2 shows that the microhardness of these compound layers is consistently between 950 and 1150 HV, which is considerably above the microhardness of 190-330 HV for the selected base alloys.

Figure 1 also reveals that the nitrocarburizing bath has actually produced multiple layers, all thinner than the seemingly coarse compound layer. These layers are especially discernable for the stainless steels: they include a dark gray top layer (e.g., on 13Cr), and in all cases but Alloy 13Cr, also a visible layer immediately beneath the compound layer, particularly on Alloys 304 and 316. Figure 2 indicates that these under-layers have a microhardness slightly below the compound layer yet relatively above the base alloys. The vertical dash lines in Fig. 2 also show the corresponding effective case depths, defined as the distance below the surface where the microhardness has dropped to 540 HVN. The effective case depths vary between 40 and 80 μm and are very much comparable to the compound layer thickness. This compound layer is relatively thick for all stainless steel samples from 40 to

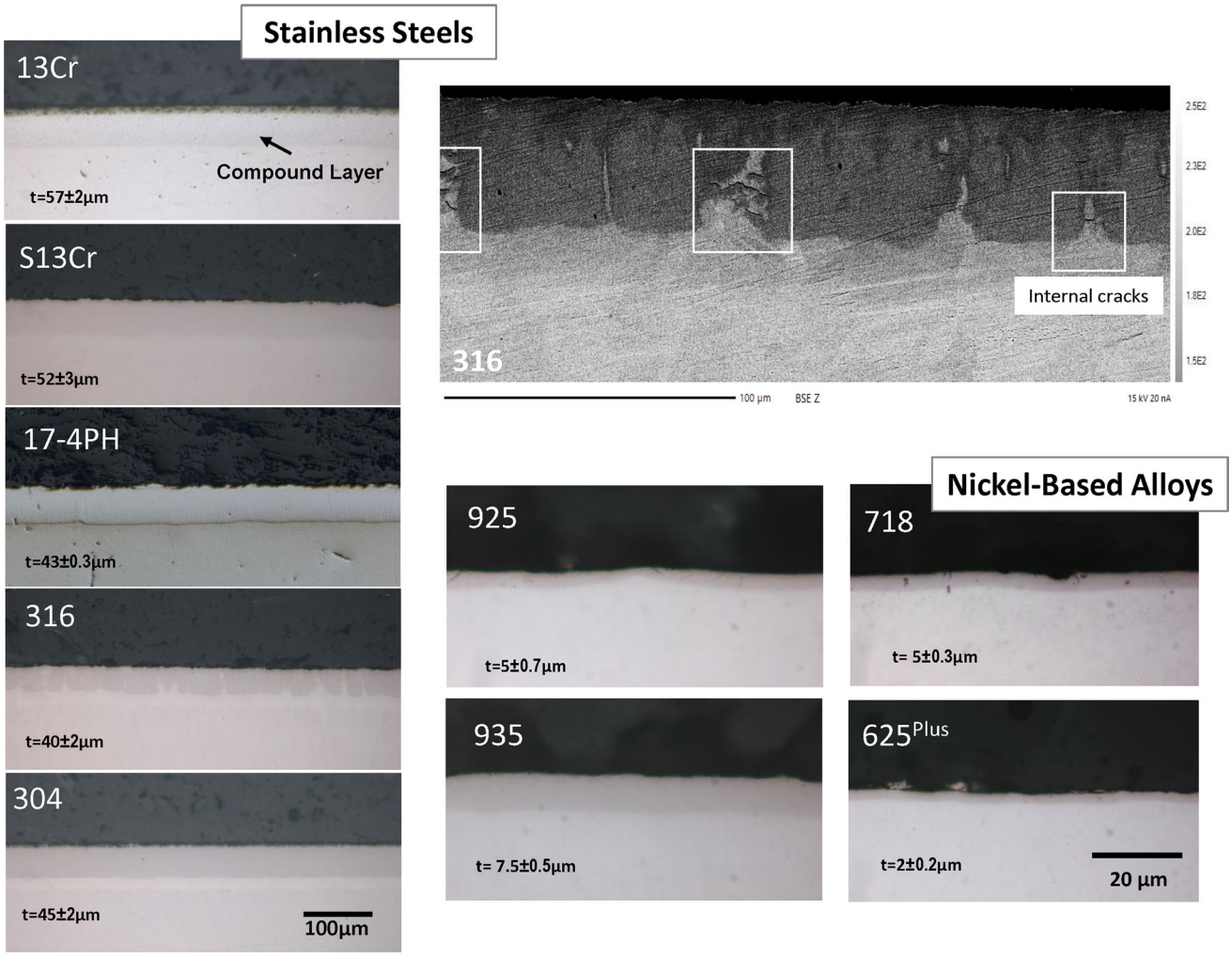

Fig. 1 Cross section microstructures of both the nitrocarburized stainless steels (e.g., 13Cr, S13Cr, 17-4PH, 304, and 316) and the nitrocarburized nickel-based alloys (e.g., 925, 935,718, and 625^{Plus}). Other layers may be observed above and below the relatively thicker compound layer. For the nitrocarburized 316 sample in particular, defects breaching through the compound layers can be observed

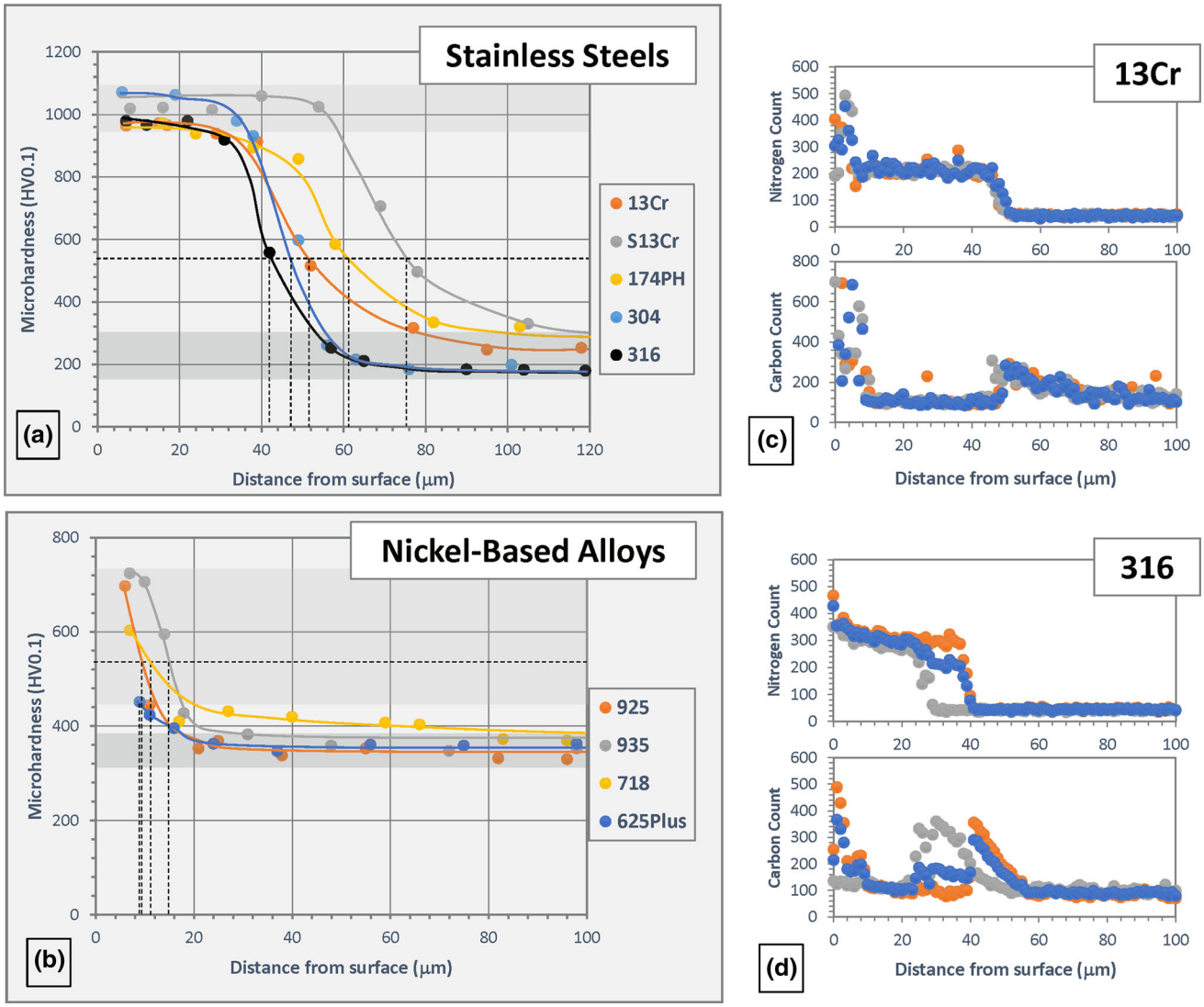

Fig. 2 Vickers microhardness profiles for (a) the stainless steels and (b) the nickel-based alloys, along with nitrogen and carbon contents measured by wavelength dispersive spectroscopy across three locations shown in different colors for (c) Alloy 13Cr and (d) Alloy 316. The superior nitrocarburizing response of stainless steels, associated predominantly with enhanced nitrogen diffusion from the surface, is greater for the leaner stainless steels and significantly reduced for the nickel-based alloys

57 μm. The thicker compound layers area observed on the 13Cr and S13Cr martensitic stainless steels. The thinner compound layers in the 304 and 316 austenitic steels are attributed to the presence of nickel and molybdenum, two elements that improve general corrosion resistance, indirectly by interfering with the formation of nitrides, or carbides (Ref 12). The resistance of nickel and molybdenum toward stabilizing nitrides is justified by the free energy values of their respective nitrides, considerably greater than that of chromium or iron nitrides (Ref 30). Since all test samples were processed altogether under a constant process cycle, the thickness variations become predominantly governed by the compositional differences, that is, the affinities of the alloying elements to stabilize nitrides, carbides, and oxides (Ref 31, 32). Figure 2 also illustrates that the introduction of nitrogen and carbon to the alloy surfaces induced a hardening well below the compound layer for the stainless steels. To assess the extent of the nitrogen and carbon diffusion, two test sample cross sections of Alloys 13Cr and 316 were line-scanned by wavelength dispersive spectroscopy at three random locations. The results are presented in Fig. 2(c) and (d). Though not absolutely quantified in percentages for lack of proper calibration standards, these two figures reveal that the nitrogen and carbon enrichments are considerable at and below the surface. The nitrogen is elevated and about constant down to a depth that matches approximately the compound layer thickness, where microhardness is also near peak values. Immediately below the compound layer, carbon content is seen to increase slightly (at about 40 μm depth) while nitrogen content keeps on decreasing to reach base alloy values ultimately. The maximum carbon content is seen at the surface and immediately below the compound layer for the two selected alloys, 13Cr and 316 alloys. The observed carbon diffusion and accumulation beyond the compound layer is consistent with previous works by M. Tsujikawa (Ref 33) and G. Li (Ref 7), disclosing that the diffusion of carbon is enhanced in the post-oxidation process as oxygen and nitrogen further displace the carbon by a competitive diffusional process (Ref 33).

Complementary examinations by scanning electron microscopy did not provide much additional insight. The image of Fig. 1 or Alloy 316 fails to disclose any clear changes in microstructure, just minor variations in contrast. As briefly discussed earlier, on each single optical image of Fig. 1, particularly for Alloy 13Cr, a darker and thinner layer was observed toward the very top. This layer becomes decreasingly visible with the stainless steels with elevated nickel or molybdenum contents and is, in fact, not optically resolvable on the nickel-based alloys, not even by scanning electron microscopy. The literature indicates that such a thin layer is caused by the post-oxidation treatment (Ref 34). On stainless steels, this post-oxidation treatment primarily aims at producing an iron oxide layer, specifically iron (III) oxide, Fe_3O_4 (Ref 34, 35). This oxide layer is not apparent on nickel-based alloys and can be explained by a shortage in available iron at the surface. The optical images of Fig. 1 also reveal that the compound layer comprises minor defects, including cracks and possibly holidays. The high-resolution SEM micrograph of Fig. 1 reveals discontinuities within the compound layer of Alloy 316. In its corresponding lower-magnification optical images, such discontinuities were also detected. Despite such imperfections, some level of corrosion protection is intuitively expected from nitrocarburizing as the formed layer provides complete coverage and is predominantly ceramic-like. This behavior, that compound and oxide layers are passive, and provide some cathodic protection until damage occurs, has been confirmed in other investigations (Ref 19, 36).

In comparison to the selected stainless steels, all nickel-based alloys exhibit a considerably thinner compound layer, with a reported thickness between 2 and 7 μm, and as low as 2 μm for Alloy 625^{Plus}. When alloy compositions are compared, those alloys rich in nickel and consequently leaner in iron under nearly identical chromium contents are the least amenable to nitrocarburizing. As previously mentioned, both chromium and iron are strong nitride formers, in contrast to nickel and molybdenum. Therefore, alloys with high nickel and molybdenum contents are generally more corrosion resistant and characterized by poor nitrocarburizing responses. In addition to chemical thermodynamic affinity, the lower diffusivity of nitrogen in the austenitic lattice of the nickel-based alloys compared to austenitic stainless steels also explains the long process times required by nickel-based alloys. Though carbon is supplied by the molten salt bath, carbon is not seen to interact with the nickel-based alloys. At the salt-bath temperature, the equilibrium phase diagrams confirm that the carbon solubility is considerably lower in the austenite of nickel-based alloys than in the austenite of stainless steels (Ref 37).

Figure 3 properly correlates compound layer thickness, as measured by optical microscopy, with both the PREN and the alloy nickel content. Among various attempted relationships, the correlation was stronger with the nickel content than with the PREN. Figure 3 quantitatively demonstrates that the compound layer decreases asymptotically with the nickel content. Alloy 17-4PH appears to be the main outlier among all alloys, showing a thinner compound layer than would otherwise be expected from the established trendline. Alloy 17-4PH also distinguishes itself by being the only alloy with noticeable about 4.0 wt.% copper. Copper does not usually stabilize either nitrides or carbides, a fact that substantiates its interference with the alloy nitrocarburizing response. This nitrocarburizing-resisting effect of copper can be described by the standard free energy of formation of copper nitride, Cu_3N,

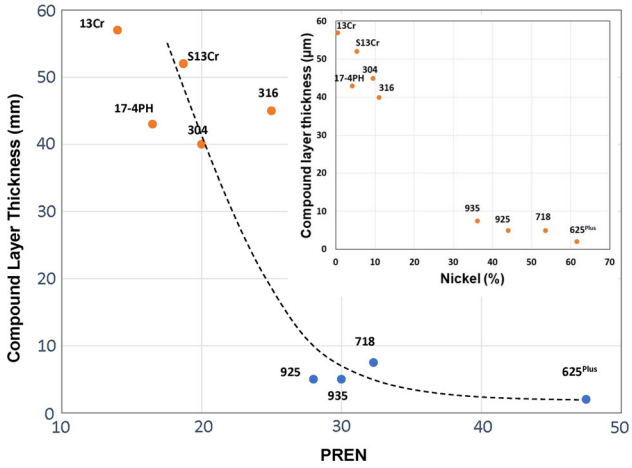

Fig. 3 Compound layer thickness Vs. nickel content and PREN. Note that Alloy 17-4PH deviates from the trendline, presumably due to the presence of copper, an element with a little chemical affinity toward nitrogen or carbon. The stainless steels are shown in orange, the nickel-based alloys in blue (Color figure online)

noticeably positive and with a value of +74.5 KJ/mol, which is in stark contrast to chromium (I) nitride, CrN at − 92 KJ/mol, molybdenum nitride, Mo_2N at -50.2 KJ/mol, or iron nitride, Fe_2N at +12.6 KJ/mol (Ref 30). Among nickel-based alloys, Alloy 718 responded more to nitrocarburizing than expected. The slightly superior response of Alloy 718 to nitrocarburizing can be attributed to niobium and tantalum, two strong nitride and carbide formers (Ref 30). A practical question that this investigation has proposed to further clarify is whether the compound layer thickness (a measure of an alloy response to nitrocarburizing) is related to corrosion resistance.

3.2 Surface Layer Characterization

For the various alloys of this investigation, Fig. 4 shows their respective x-ray diffraction patterns in both un-nitrocarburized and nitrocarburized conditions. The X-ray patterns for the un-nitrocarburized stainless steels characteristically reveal the presence of the equilibrium iron phases, α-Fe and γ-Fe; after nitrocarburizing, the dominant x-ray peaks turned out to be associated to iron (III) oxide, Fe_3O_4, which may be explained by the post-oxidation process. In all appearance, this iron oxide layer acts as a protective shield against the proper detection of nitrogen and carbon phases from underneath. Elsewhere, it has been reported that several nitride compounds of various stoichiometries are present, among which are iron (II/III) nitride, $Fe_{2-3}N$, iron (IV) nitride, Fe_4N, and chromium (I) nitride, CrN (Ref 20). Chromium (I) nitride, CrN, is known to form at nitrocarburizing temperature of 580 °C, as inferred both by its lowest free energy of formation, and the relative low diffusivity of chromium into iron at a temperature in excess of 450 °C (Ref 38).

The x-ray diffraction patterns for the un-nitrocarburized and nitrocarburized nickel-based alloys are also depicted in Fig. 4 and can be compared to the stainless steels. Test samples of Alloys 925, 935, 718, and 625^{Plus} all point out at the austenite γ-phase; their nitrocarburized counterparts are observed to only show the austenite phase and the chromium (I) nitride phase, CrN. This finding is quite in contrast with the un-nitrocarburized stainless steels, where diffraction peaks of iron (III) oxide,

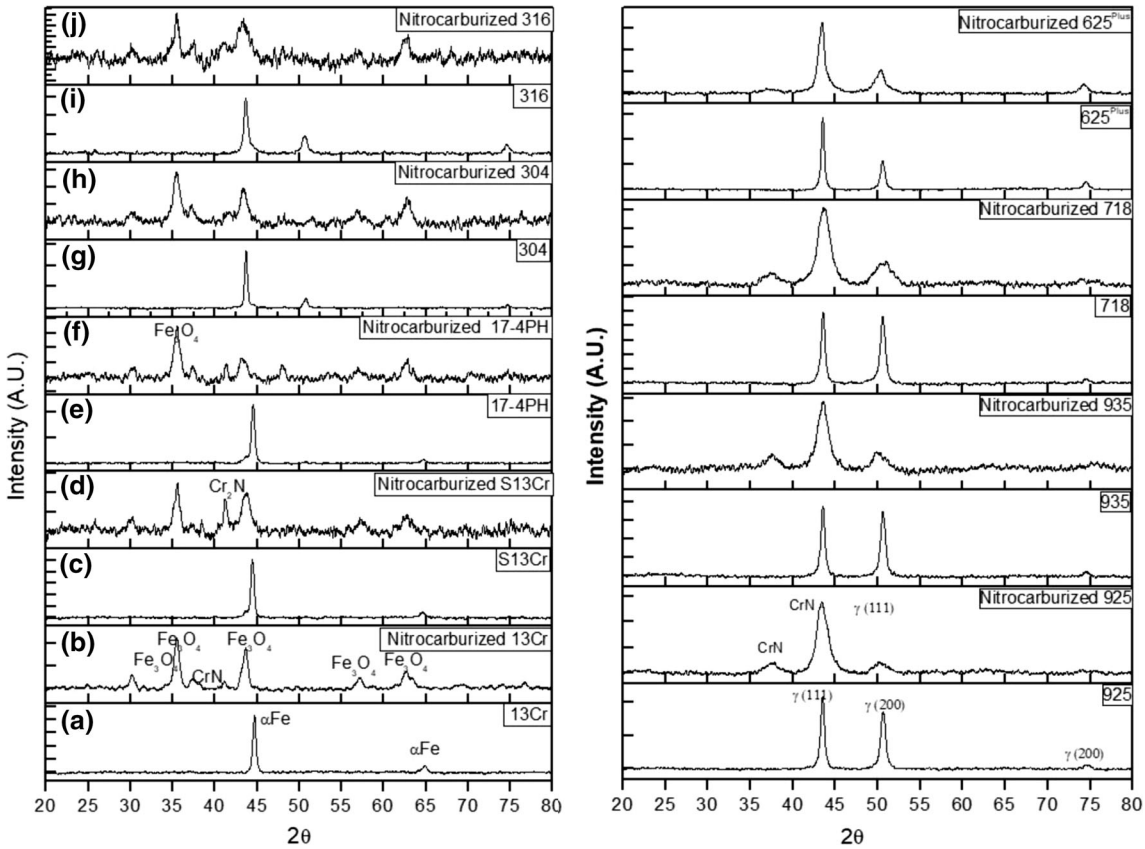

Fig. 4 Sets of x-ray diffraction patterns for both un-nitrocarburized and nitrocarburized alloys. The nickel-based alloys show a more moderate response toward nitrocarburizing, in line with the observations of Fig. 1, 2

Fe_3O_4 were identifiable. The lack of a perceptible surface oxide film on the nickel-based alloys is first explained by a shortage of free iron, and second, the general and well-established fact that nickel-based alloys are simply more oxidation resistance (Ref 23). As already discussed, and in the absence of suitable thermodynamic conditions to promote nitrides of nickel, the compound growth is predominantly controlled by the much stronger nitride formers, chromium, and iron. As anticipated by its lower nickel and greater iron content, the nitride layer on Alloy 935 is marginally thicker than in Alloys 925 or 625^{Plus}. Finally, for all alloys, the introduction of nitrogen results in broader diffraction peaks, as exemplified by the nickel alloys. These peak broadening infer that the original phases have been expanded, that is interstitially enriched, resulting in lattice expansion. When not accompanied by nitride sensitization (no indication found), the nitrogen enrichment of either the α-Fe or γ-Fe phases would cause significantly increased values in PREN. It follows that the alloy under the compound layer could offer enhanced general corrosion resistance, a feature that is probably meaningful in the presence of a defective compound layer.

3.3 Cyclic Potentiodynamic Polarization

Figure 5 and 6 show the cyclic polarization curves of the stainless steels in 3.5 wt.% sodium chloride brine for the un-nitrocarburized and nitrocarburized conditions, respectively. For a subsequent and more quantitative discussion, electrochemical parameters such as open-circuit potential (OCP), corrosion potential (E_{corr}), corrosion current (I_{corr}), critical pitting potential (E_{pit}), and re-passivation potential (E_{rep}) were also extracted from the analysis of polarization curves and summarized in Table 3. First note that the two potentials, OCP and E_{corr}, are well correlated and yet are still quite distinct given that the OCP is established under conditions approaching thermodynamic equilibrium. Figure 7 plots explicitly E_{corr} Vs. OCP in an attempt to broadly visualize the departure between the two potentials. It is now seen that the two potentials are indeed highly correlated and near each other at an ideal 1:1 ratio for the un-nitrocarburized alloys; however, for the nitrocarburized alloys, the E_{corr} values are on average trailing the OCP by about 100 mV, clearly indicating that the nitrocarburizing layer for the stainless steels and nickel alloys indistinctively create an overpotential that is to be overcome for the corrosion current to increase. Despite differences, Fig. 7 validates that OCP and E_{corr} can be discussed interchangeably. Among electrochemical parameters, E_{corr} has been given an extra attention along E_{pit} because the difference between E_{pit} and E_{corr} directly measures the stability of the passive film.

The un-nitrocarburized stainless steels are characterized the classic cyclic polarization profiles with positive hysteresis loop and variable re-passivation abilities. Figure 5(a) shows that the E_{corr} values are approximately identical and in the vicinity of − 180 mV. The pitting potentials are also similar for Alloys 13Cr and S13Cr and noticeably smaller than for Alloys 17-4PH, 304, and 316. Furthermore, when the potentials are eventually reduced, both Alloys 13Cr and S13Cr are not observed to re-passivate. These results are somewhat predictable: the higher pitting potentials of Alloys 304 and 316 can

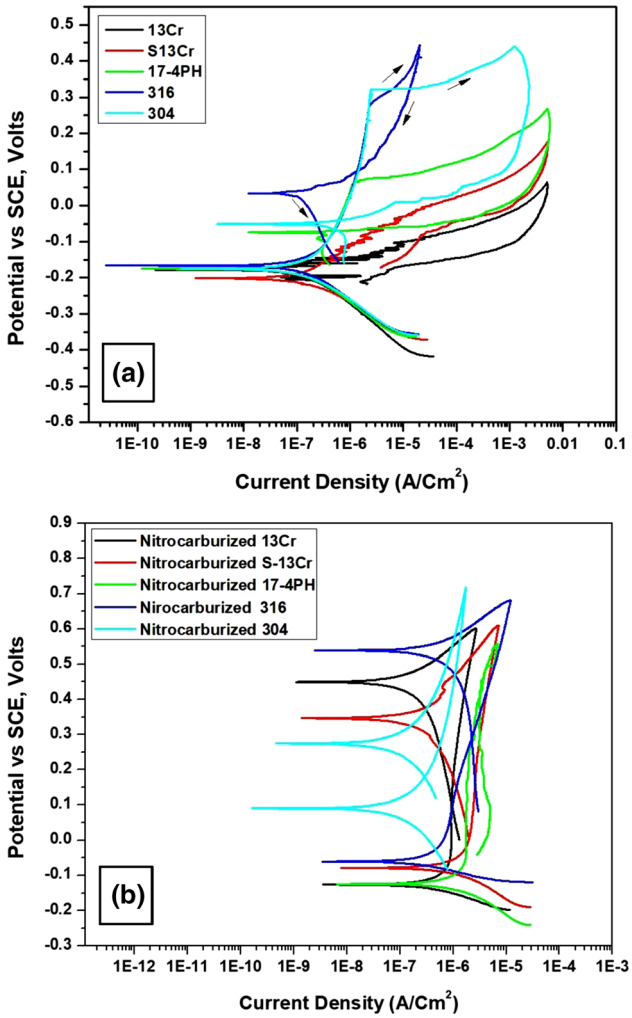

Fig. 5 Cyclic potentiodynamic polarization plots for stainless steels in 3.5 wt% NaCl solution: (a) un- nitrocarburized and (b) after nitrocarburizing for Alloys 13Cr, S13Cr, 17-4PH, 304, and 316

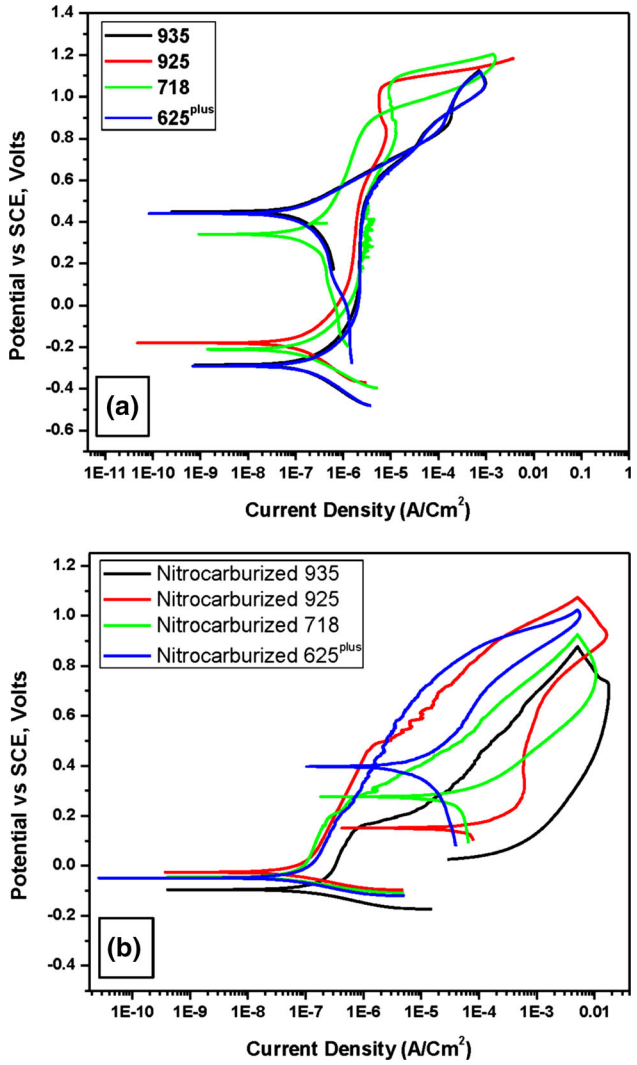

Fig. 6 Cyclic potentiodynamic polarization plots of nickel-based alloys in 3.5wt% NaCl solution: (a) un- nitrocarburized, and (b) after nitrocarburizing for Alloys 925, 935, 718, and 625Plus

be simplistically explained by their PREN values, as reported in Table 1, while the lack of re-passivation of Alloys 13Cr and S13Cr can be explained by the scans, terminated too early without reaching lower potentials.

The cyclic polarization curves for the nitrocarburized stainless steels are captured in Fig. 5(b) and are strikingly different from their counterparts in Fig. 5(a). With the exception of the nitrocarburized 17-4PH alloy, the nitrocarburized stainless steels of Fig. 5(b) commonly exhibit negative hysteresis loops. The E_{corr} values are also clustered near − 100 mV. In contrast to the un-nitrocarburized alloys, the pitting potentials, E_{pit}, were not appropriately measured because of overpotential limits imposed by the scan settings. However, it is clear that all pitting potentials are greater than encountered for the un-nitrocarburized alloys, with a minimum value of 535 mV recorded for nitrocarburized Alloy 17-4PH. This shift in E_{corr} and E_{pit} toward a more passive behavior indicates an improvement in corrosion resistance under the conditions set by this investigation. The reverse curves for the nitrocarburized stainless steels also disclose a lower current density, implying that the compound layer offers some level of corrosion protection. In the literature, T. Borowski et al. have reported that nitrocarburizing process raised the pitting potential of stainless steels, while the nitride layer reduces chemical attacks by chloride ions (Ref 36). In this corrosion investigation on a nitrocarburized 316L alloy, the pitting potential was seen to increase by 1.5V in an equivalent chloride environment (e.g., 3.5 wt%NaCl), resulting in another improved passive range. The latter has been explained by chemical changes occurring at the surface of nitrocarburized stainless steels, specifically the surface segregation of a negatively charged nitrogen converted according to reaction (1) below (Ref 39, 40).

$$N^{3-} + 4H^{+} \rightarrow NH_4^{+} \quad \text{(Eq 1)}$$

$$2H^{+} + 2e^{-} \rightarrow H_2 \quad \text{(Eq 2)}$$

$$Fe \rightarrow Fe^{2+} + 2e^{-} \quad \text{(Eq 3)}$$

As per this proposed model, the produced ammonium ions remain toward the top layers of the surface and contribute toward neutralizing the acidic pit environments (Ref 39). As a result of hydrogen cation consumption, the localized pH increases, at least partially inhibiting the hydrogen reaction

Table 3 Cyclic polarization results for all investigated alloys in 3.5wt% sodium chloride solution at ambient temperature before and after nitrocarburizing

	As received or un-nitrocarburized alloys						Nitrocarburized alloys					
Alloys	**OCP**	E_{corr}	I_{corr}	E_{pit}	E_{rep}	$E_{pit} - E_{corr}$	**OCP**	E_{corr}	I_{corr}	E_{pit}	E_{rep}	$E_{pit} - E_{corr}$
13Cr	− 218	− 178	1.30	− 127	NA	51	18	− 126	2.8	600	450	726 min
S13Cr	− 171	− 202	0.79	− 130	NA	72	9	− 78	12	600	350	678 min
17-4PH	− 165	− 176	1.87	61	70	237	− 41	− 124	9	535	495	659
304	− 156	− 166	1.49	279	95	445	117	90	2.55	> 700	274	610 min
316	− 159	− 175	1.10	321	-42	496	80	− 60	2.3	> 700	539	760 min
935	− 275	− 284	0.83	> 1000	945	1284 min	25	− 96	1.04	140	NA	236
925	− 169	− 180	0.98	> 1000	NA	1180 min	102	− 26	0.465	462	NA	488
718	− 196	− 211	0.75	> 1000	941	1211 min	91	− 46	0.439	193	276	239
625^{Plus}	− 280	− 290	0.63	> 1000	945	1290 min	79	− 49	0.532	650	401	699

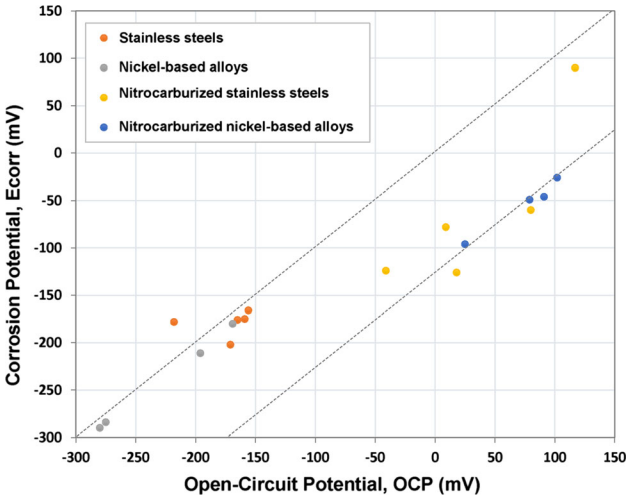

Fig. 7 The corrosion potential, Ecorr, Vs. open-circuit potential, OCP, for stainless steels and nickel-based superalloys in un-nitrocarburized and nitrocarburized conditions

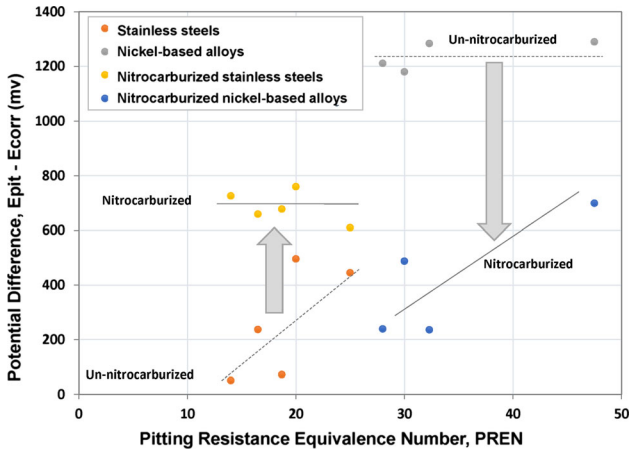

Fig. 8 Potential difference, $E_{pit} - E_{corr}$, Vs. pitting resistance equivalent number, PREN, for both the un-nitrocarburized and the nitrocarburized stainless steels and nickel-based alloys

(2) and equivalent anodic reaction (3) thus reducing the iron dissolution.

Figure 6(a) and (b) depicts the cyclic polarization curves for all four nickel-based alloys in both un-nitrocarburized and nitrocarburized conditions. Like the stainless steels, the nickel-based alloys are also characterized by the usual polarization curves (Fig 6a), i.e., an initial low-current density such as I_{corr} followed by a steep potential increase indicative of a stable passive state, as defined by a wide range between E_{Pit} and E_{corr}. As shown by Fig. 6(b), nitrocarburizing reliably raises the E_{corr} values for all four nickel-based alloys while significantly lowering pitting potential, E_{pit}. The polarization curves of Fig. 6(b) further disclose that the nitrocarburized alloys remained in a passive state but corroded at a lower potential than in their un-nitrocarburized condition. The polarization plots also show rapid increases in the corrosion current density, I_{corr}, with increasing potentials, the first evidence that nitrocarburizing these alloys negatively influences corrosion resistance.

To better comprehend the effects of nitrocarburizing on stainless steels and nickel-based alloys, the results of Fig. 5 and 6 are revisited in Table 3, where several characteristics of the polarization plots have been consolidated for side-by-side comparisons and then replotted in Fig. 7 and 8. With both open-circuit potential, OCP, and corrosion potential, E_{corr}, already addressed, some attention is reoriented toward the current, I_{corr}. First, the values of I_{corr} are consistently lower for the nickel-based alloys and noticeably greater for the nitrocarburized stainless steels than their un-nitrocarburized counterparts. For the nickel-based alloys, the corrosion current, I_{corr} is not considerably influenced by nitrocarburizing. The higher I_{corr} values suggest that more corrosion should simply be expected from the nitrocarburized stainless steel. Figure 7 shows the comparison of E_{corr} and OCP for stainless steels and Ni- alloys in both conditions. This confirms that the E_{corr} and OCP values have improved with the nitrocarburizing process.

To complement this analysis, pitting potentials, E_{pit}, and E_{corr}, are also examined more comprehensively with Fig. 8, where the difference of potentials between E_{pit} and E_{corr} is represented against the PREN, used a single and convenient measure of the cumulative effect of the main alloying elements. Recall that this difference in potentials has been proven to be a good measure of the alloy passivity, as discussed elsewhere (Ref 41). Even though the data are occasionally scattered, Fig. 8 enables to clearly separate the stainless steels and the nickel-based alloys in their nitrocarburizing responses. When nitrocarburized, the stainless steels and the nickel-based alloys follow opposite directions. The stainless steels' ability to remain passive (represented by their $E_{pit} - E_{corr}$ values) is

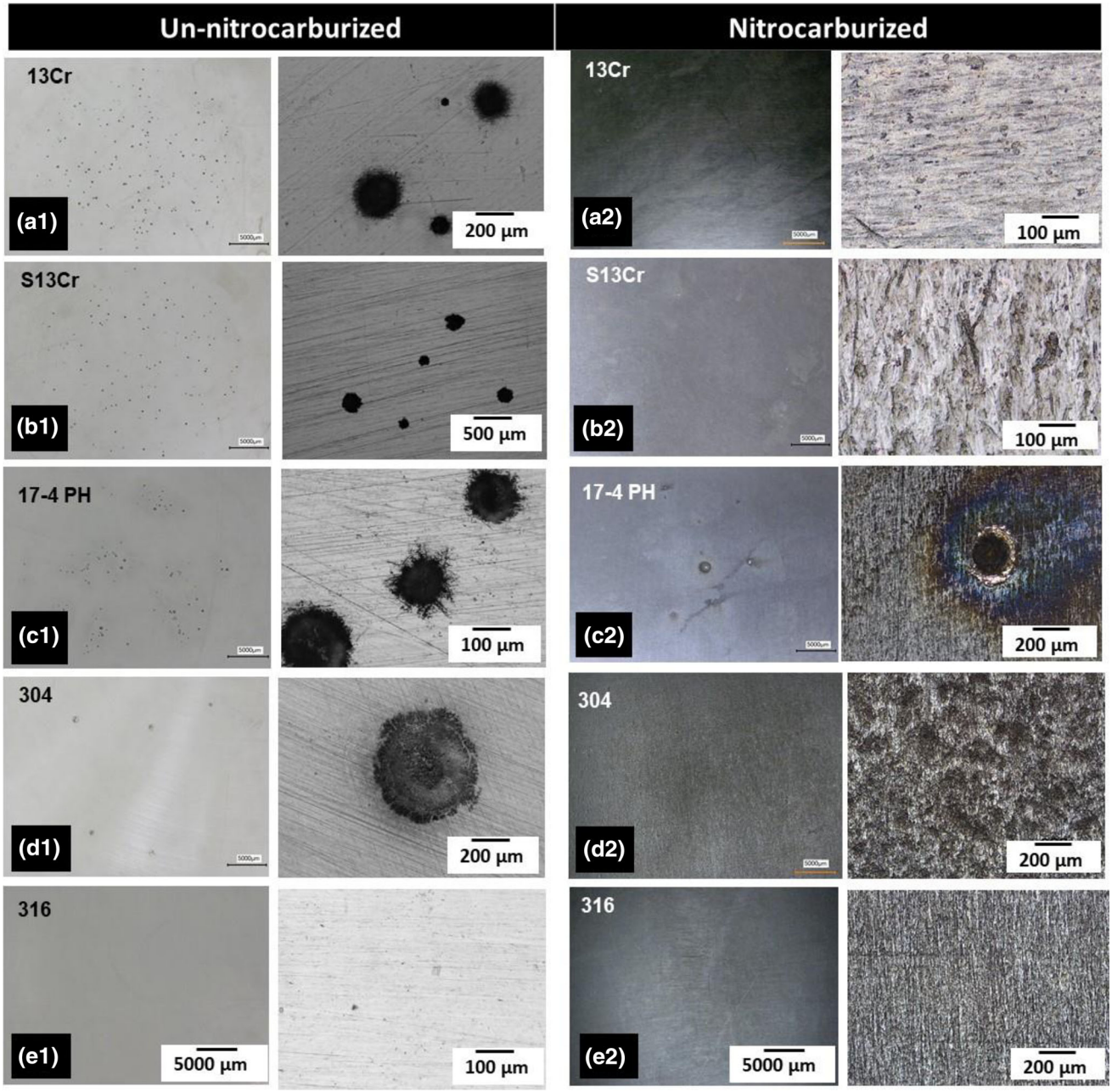

Fig. 9 Laser confocal photomicrographs of the cyclic polarization tested surfaces of both un-nitrocarburized (a1-e1, left) and nitrocarburized stainless steel test samples (a2-e2, right). Figure a1-e1 present low- and high-magnification micrographs showing corrosion pits. Figure (a2-e2) reveal no pitting after nitrocarburizing with exception of a few on the nitrocarburized 17-4PH alloy

raised after nitrocarburizing. This improvement is particularly substantial for alloys having low PREN values, such as the non-austenitic stainless steels (i.e., 13Cr, S13Cr, 17-4PH). These alloy's enhanced region of passivity can be explained by their thicker compound layers after nitrocarburizing. For the nickel-based alloys, all alloys appear to possess a comparable passive range in the 3.5wt.% sodium chloride solution at ambient temperature, while the passive range of their nitrocarburized surfaces is seen to fall dramatically to levels comparable to stainless steels with a minimum PREN value of approximately 20. The reduction in passive range is major for the nickel-based alloys, and decreases with the alloy PREN values. Through positive influence on PREN, alloying elements such as chromium and molybdenum thus at least partially offset the effects of nitrocarburizing by promoting a stable region of passivity.

The apparent reduction in corrosion resistance observed for the nickel-based alloys is confirmed by the re-passivation potentials, E_{rep}. Though inconsistently available, the nitrocarburized stainless steels show much improved re-passivation potentials that predictably increase with the alloy PREN value. In contrast, for the nickel-based alloys, the trend is entirely opposite. These results from complementary and independent electrochemical parameters all point toward two distinct and differing effects of nitrocarburizing: (1) the stainless steels offer a generally increased corrosion resistance, at least temporarily

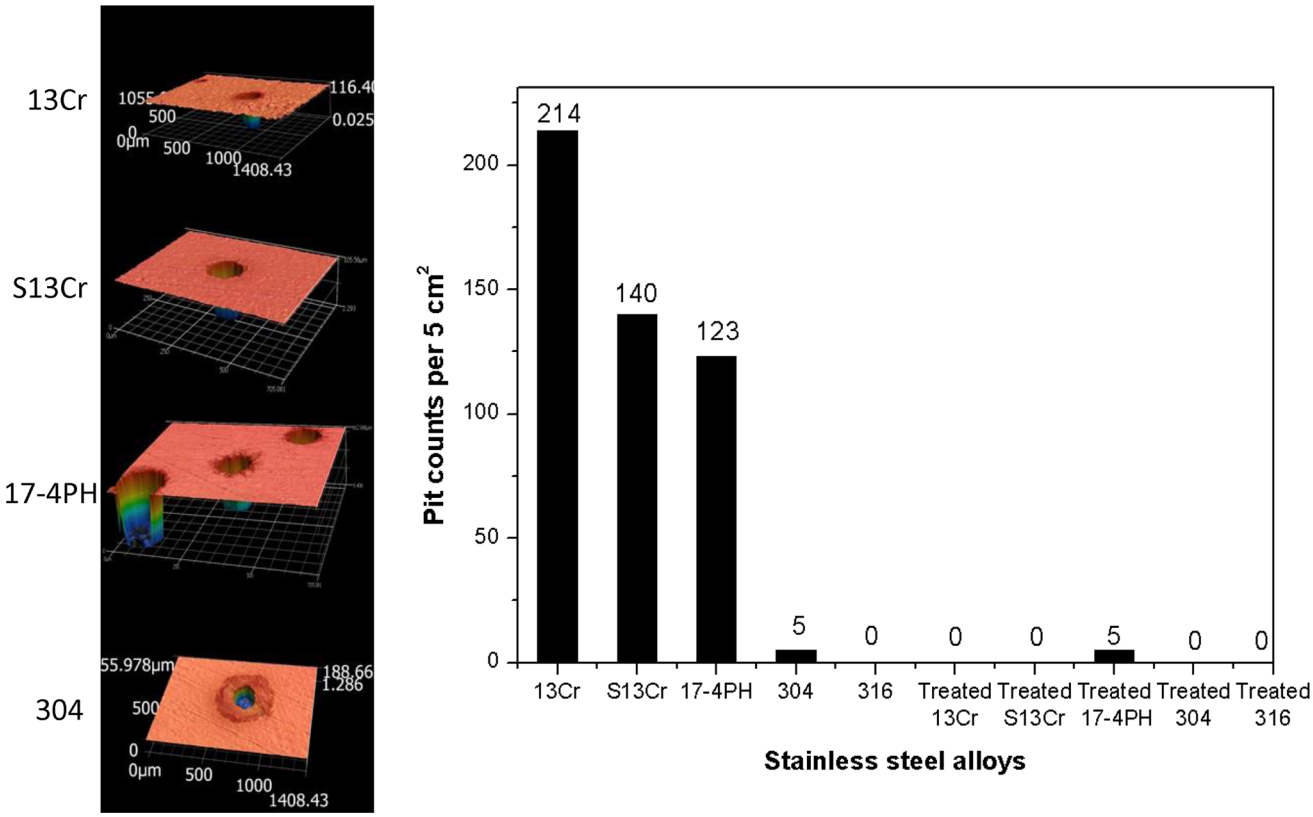

Fig. 10 Pit population count (density) for the stainless steel test samples in both un-nitrocarburized and nitrocarburized conditions (right). Selected 3D pit profiles are depicted on the left for several un-nitrocarburized stainless steels, specifically Alloys 13 Cr, S13Cr,1 7-4PH, and 304.

and until oxide and compound layers are breached, and (2) all investigated nickel-based alloys lose some levels of protectiveness or corrosion resistance simply because of a reduced ability to re-passivate and thus avoid dissolution.

3.4 Surface Examination

Following cyclic potentiodynamic testing, all tested and available surfaces were thoroughly examined for quantitative evidence of corrosion, particularly pitting, but also general corrosion (dissolution), as promoted by the use of large overpotentials with several alloys now proven to have reduced passive range (e.g., nickel-based alloys). Figure 9 provides a set of optical micrographs of the various alloy surfaces in their un-nitrocarburized and nitrocarburized conditions, vertically organized by increasing PREN value from Alloys 13Cr to 316. In Fig. 9, the left images were consistently captured at an identical magnification and are completed on their right by close-up views to facilitate comparisons. First, spherical pits are clearly not uncommon, and their occurrence depends on the alloy PREN. Figure 9 specifically illustrates that a greater PREN value leads to a lower pit density population. For instance, Alloys 13Cr and S13Cr, with respective PREN of about 14.0 and 18.7, have the greatest pit populations (Fig. 9a1-b1). The laser confocal microscopic analyses reveal that these pits are generally in excess of 100 μm in width and depth. Comparatively, Alloy 17-4PH exhibits a very moderate pitting (Fig. 9c1), even though some pits were as coarse as in other alloys. Alloy 304 discloses a surface with very sporadic pitting (Fig. 9d1), while Alloy 316 (Figure 9e1) remained totally free of any visible pits. In general, as described by Fig. 9, the occurrence of pitting can be related to the peak currents recorded and disclosed in Fig. 5. Specifically, the alloys exhibiting minor pitting are also the alloys that have generated the least currents, many separated by orders of magnitudes.

For all stainless steel surfaces, Fig. 10 reports their measured pit counts over an analyzed surface of 5.0 cm^2, as determined through quantitative image analyses. Despite the pit count decreasing quasi-exponentially with alloy PREN, nitrocarburizing is confirmed to produce a more pitting resistant surface, with only a single and sporadic visible pit on the nitrocarburized 17-4PH alloy. These observations agree entirely with Fig. 8, where any surface characterized by a difference of potentials over 400 mV appears to be immune to pitting. In a broader context, the corrosion resistance of a nitrocarburized surface cannot be directly related to its compound layer, or other layers previously identified in this paper. All compound layers, mainly for the stainless steels, act as barriers that raise the potential required for pitting by about 700 mV above the corrosion potential; however, this barrier is also defective, as suggested by Fig. 2. Furthermore, as disclosed by Fig. 9(c1) and (c2), microcracks and perhaps holidays may not be that uncommon in these compound layers, and these surely impacts corrosion as it develops (Ref 42).

Figure 11 depicts similar optical images for the nitrocarburized nickel-based alloy surfaces. The un-nitrocarburized alloys show limited pitting, including Alloys 925 and 718, where the test sample outer perimeters predominantly clustered pits. Pitting was absent on Alloys 935 and 625^{Plus}, the two alloys with the largest PREN values. Though pitting was

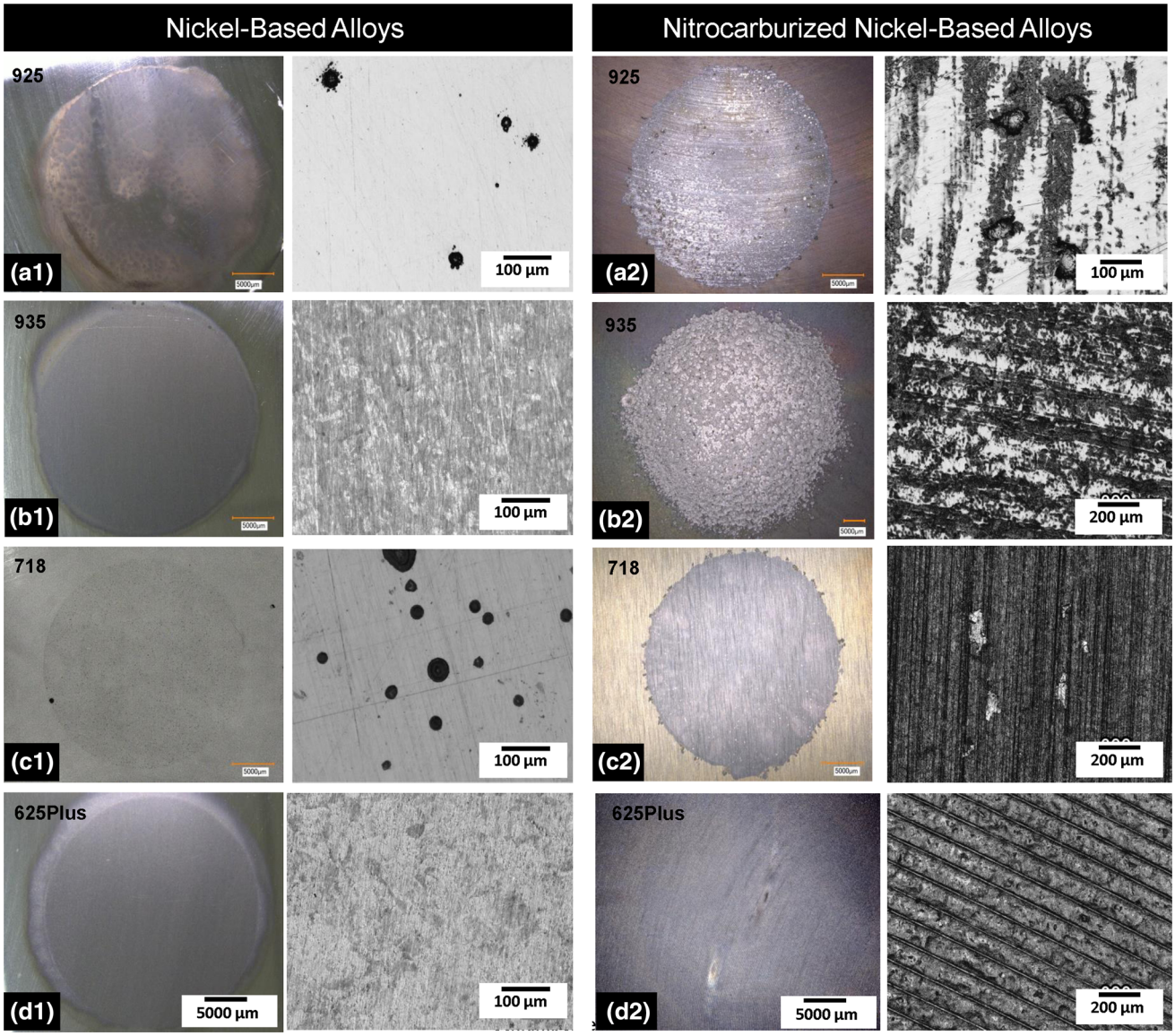

Fig. 11 Laser confocal photomicrographs of the surfaces of the un-nitrocarburized (a1-to-d1, left) and the nitrocarburized (a2-d2, right) nickel-based alloys after cyclic polarization testing. Pits are observed only on Alloys 925 and 718 in the un-nitrocarburized condition. Figure (a2) and (b2) show major losses (in compound layer) for Alloys 925 and 935, respectively.

absent, the nitrocarburizing of Alloys 925 and 935 resulted in superficial dissolution, as indicated by the darker regions of Fig. 11(a2)-(b2). In the nitrocarburized Alloy 925, the pits are considerably deeper (57-65 μm) than in the nitrocarburized Alloy 935 (1-4 μm), where the dissolution is marginally more pronounced. The nitrocarburized Alloy 718 also experienced some minor pitting, with a total of 57 pits over the test surface, with a range of depths between 3 and 7 μm. Following potentiodynamic testing, the nitrocarburized Alloy 718 were observed to spall small flakes, as captured by Fig. 11(c2). In neither the un-nitrocarburized nor the nitrocarburized conditions, Alloy 625^{Plus} experienced any obvious pitting; however, the dissolution of thin nitrides before the re-passivation occurred because of the high potential scans.

Figure 12 presents three secondary electron images and a back-scattered electron image of microscopic pits (50-μm) found upon scanning the nitrocarburized surface of Alloys 925 and 935. The images reveal preferential grain-boundary attacks, the normal initiation site for pitting also seen on the un-nitrocarburized alloys. The nitrocarburized Alloy 935 also depicts a corrosion byproduct, most noticeable on the back-scattered image. In the context of Fig. 1, pitting under the compound layer should be expected, predominantly where the compound layer is discontinuous, for instance, at microcracks such as shown in Fig. 1. Though carbon and nitrogen can potentially be a root cause for alloy sensitization (i.e., carbide and/or nitride formation along the alloy grain boundaries), no such evidence has been found in this investigation. At the same time, there is no clear evidence in the literature for stainless steels sensitization occurring below a thin nitrocarburized layer, which may be the result of the short nitrocarburizing cycles and relatively low temperatures associated with molten salt processes.

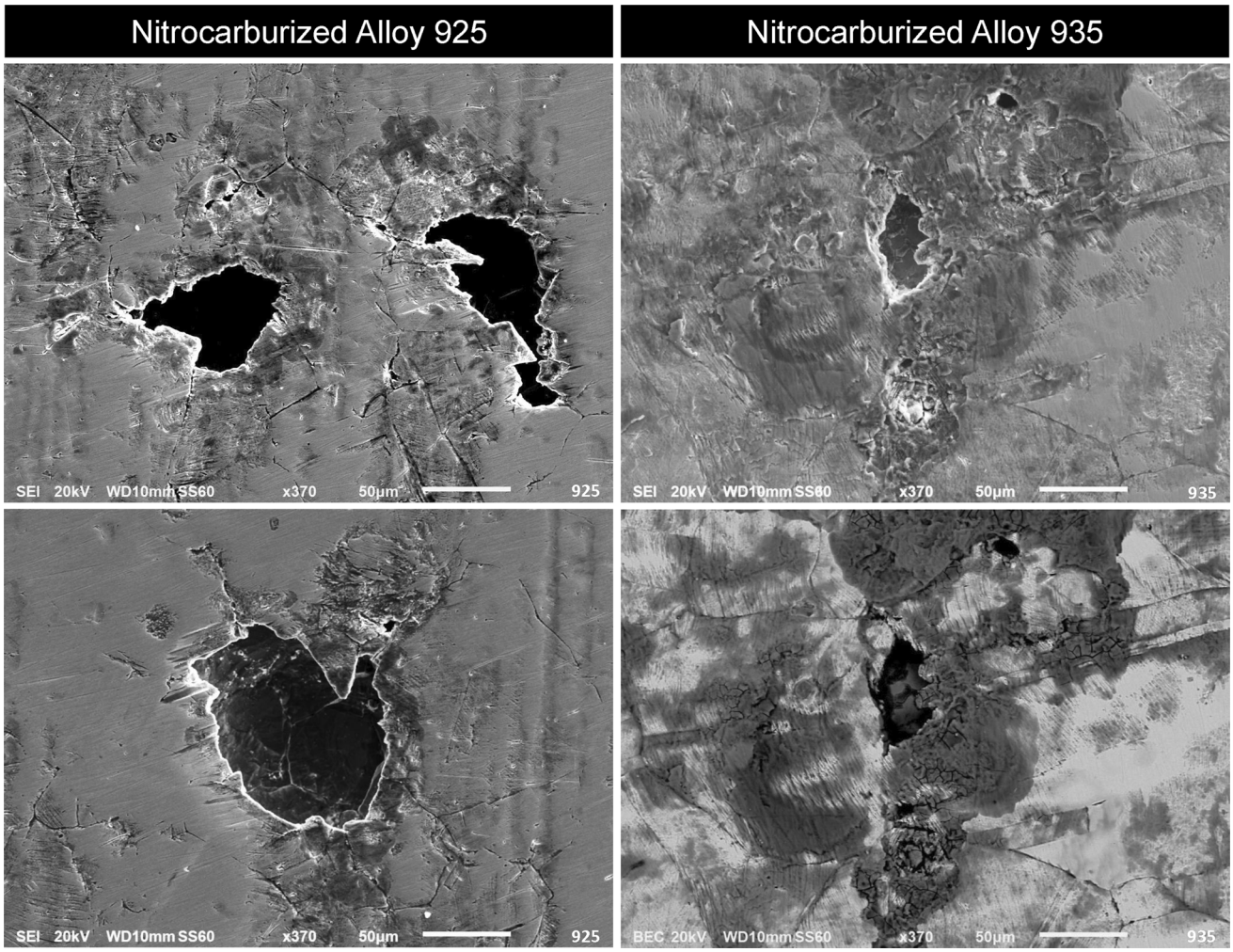

Fig. 12 Scanning electron micrographs of the nitrocarburized 925 and 935 surfaces. The surfaces had been gently polished off to reveal the compound sublayer.

4. Conclusions

This investigation includes a broad range of high-chromium stainless steels and nickel-based alloys in use for hydrocarbon production, carbon sequestration, and subterranean geothermal environments, and as such is highly relevant to better understand the effects of nitrocarburizing on all these common alloys, particularly when exposed to corrosion. Specifically, this investigation has clarified the effects of nitrocarburizing after short-term exposures to a light 3.5 wt.% sodium chloride brine at ambient temperature. As such it remains far from providing sufficient arguments to justify the long-term performance of nitrocarburizing in actual field environments. First, salt-bath nitrocarburizing is confirmed to significantly increase surface hardness through the formation of nitride compounds on both the stainless steels and the nickel-based alloys. As a general trend, stainless steels are characterized by deeper case depths and thicker compound layers than the nickel-based alloys, as well explained and correlated to their nickel contents and PREN values. On all stainless steels, thin oxide films were also detected covering the compound layers, and despite the presence of defects (microcracks, holidays) in the compound layers, no indication of reduced corrosion resistance was found. On the contrary, all the tested nitrocarburized stainless steels resisted corrosion, as explained by their relatively thick and passive nitride compound layers. Recall that for all stainless steels, not only their open-circuit potential, pitting potential, and re-passivation potential was increased, but also their passive range. In contrast to the tested stainless steels, the salt-bath nitrocarburizing of nickel-based alloys produced thin compound layers that are consistently associated with reduced pitting potentials, reduced re-passivation potentials, a narrower passive range, thus overall a decrease in corrosion resistance. After nitrocarburizing, and upon being scanned above their pitting potentials, all nickel-based alloys exhibited some degrees of anodic dissolution, reaching beyond the compound layer. Among all alloys, remarkably, pitting was not observed on Alloy 625^{Plus} in either un-nitrocarburized or nitrocarburized conditions. Upon nitrocarburizing, the corrosion resistance of all nickel alloys was certainly reduced; however, in context, this reduction is limited and apparently comparable to stainless steels with a minimum PREN in the vicinity of 20. At last, the presence of nitrogen and carbon below the compound layer, though not entirely clarified, increases PREN in the two austenitic alloys through so-called expanded austenite (austenite with increased interstitial nitrogen and carbon solubility). This localized enrichment in nitrogen, and to some extent

carbon, may also have a positive austenite forming stabilizing effect in the other stainless steels. For the nickel-based alloys, nitrogen and carbon solubilities are relatively insignificant, and therefore no such effect is anticipated. The specific roles of interstitial elements such as carbon and nitrogen certainly deserve complementary investigations. Above all, the long-term performance of nitrocarburized surfaces of both stainless steels and nickel-based alloys remains in need of further assessments, particularly to determine if and how short-term electrochemical results translate into longer-term corrosion resistance.

References

1. D.L.F. Ajit K. Roy and Beverly Y. Lum, 98157 Stress Corrosion Cracking OF Fe-Ni-Cr-Mo, Ni-Cr-Mo AND Ti Alloys IN 90°C Acidic Brine, Corrosion 98, p. NACE-98157, 1998
2. Petroeum and Natural Gas Industries-Materials for Use in H_2S Containing Environments in Oil and Gas Production, NACE, MR0175/ISO 15156, 2015
3. V. Singh, and M. Marya, On the Corrosion Resistance of Nitrocarburized and Boronized Nickel-based Alloys, *Materials Science & Technology Conference and Exhibition 201 (MST'19)*, 2019, p. 319–326
4. V.S. Manuel Marya, Y. Chen and H. Liang, On the Friction and Anti-Galling Properties of Coatings and Surface Treatments, *Materials Science & Technology Conference and Exhibition* 2019, p. 364–371
5. H. Xiang, G. Wu, D. Liu, H. Cao and X. Dong, Effect of Quench Polish Quench Nitriding Temperature on the Microstructure and Wear Resistance of SAF2906 Duplex Stainless Steel, *Metals*, 2019, **9**(8), p 848
6. A. Gunen and E. Kanca, Microstructure and Mechanical Properties of Borided Inconel 625 Superalloy, *Matéria (Rio de Janeiro)*, 2017 https://doi.org/10.1590/s1517-707620170002.0161
7. G.-J. Li, Q. Peng, J. Wang, C. Li, Y. Wang, J. Gao, S.-Y. Chen and B.-L. Shen, Surface Microstructure of 316L Austenitic Stainless Steel by the Salt Bath Nitrocarburizing and Post-oxidation Process Known as QPQ, *Surf. Coat. Technol.*, 2008, **202**(13), p 2865–2870
8. S.P. Brühl, R. Charadia, S. Simison, D.G. Lamas and A. Cabo, Corrosion Behavior of Martensitic and Precipitation Hardening Stainless Steels Treated by Plasma Nitriding, *Surf. Coat. Technol.*, 2010, **204**(20), p 3280–3286
9. L.C. Gontijo, R. Machado, E.J. Miola, L.C. Casteletti, N.G. Alcântara and P.A.P. Nascente, Study of the S Phase Formed on Plasma-nitrided AISI 316L Stainless Steel, *Mater. Sci. Eng., A*, 2006, **431**(1), p 315–321
10. A. Fossati, F. Borgioli, E. Galvanetto and T. Bacci, Corrosion Resistance Properties of Glow-Discharge Nitrided AISI 316L Austenitic Stainless Steel in NaCl Solutions, *Corros. Sci.*, 2006, **48**(6), p 1513–1527
11. L.B. Winck, J.L.A. Ferreira, J.A. Araujo, M.D. Manfrinato and C.R.M. da Silva, Surface Nitriding Influence on the Fatigue Life Behavior of ASTM A743 Steel Type CA6NM, *Surf. Coat. Technol.*, 2013, **232**, p 844–850
12. ASM Handbook, Volume **5**: Surface Engineering, 1994
13. T. Makishi and K. Nakata, Surface Hardening of Nickel Alloys by Means of Plasma Nitriding, *Metall. Mater. Trans. A.*, 2004, **35**(1), p 227–238
14. Y. Sun, Kinetics of Layer Growth During Plasma Nitriding of Nickel Based Alloy Inconel 600, *J. Alloy. Compd.*, 2003, **351**(1), p 241–247
15. J. Alphonsa, V.S. Raja and S. Mukherjee, Study of Plasma Nitriding and Nitrocarburizing for Higher Corrosion Resistance and Hardness of 2205 Duplex Stainless Steel, *Corros. Sci.*, 2015, **100**, p 121–132
16. F.M. Arash Maniee and R. Soleimani, Improved Hardness, Wear and Corrosion Resistance of Inconel 718 Treated by Hot Wall Plasma Nitriding, *Metals Mater. Int.*, 2019, **26**, p 1664
17. N. Makuch and M. Kulka, Microstructural Characterization and Some Mechanical Properties of Gas-Borided Inconel 600-Alloy, *Appl. Surf. Sci.*, 2014, **314**, p 1007–1018
18. T. Borowski, A. Brojanowska, M. Kost, H. Garbacz and T. Wierzchoń, Modifying the Properties of the Inconel 625 Nickel Alloy by Glow Discharge Assisted Nitriding, *Vacuum*, 2009, **83**(12), p 1489–1493
19. F.A.P. Fernandes, L.C. Casteletti and J. Gallego, Microstructure of Nitrided and Nitrocarburized Layers Produced on a Superaustenitic STAINLESS Steel, *J. Market. Res.*, 2013, **2**(2), p 158–164
20. G.-J. Li, J. Wang, Q. Peng, C. Li, Y. Wang and B.-L. Shen, Influence of Salt Bath Nitrocarburizing and Post-oxidation Process on Surface Microstructure Evolution of 17–4PH Stainless Steel, *J. Mater. Process. Technol.*, 2008, **207**(1), p 187–192
21. L. Li, J. Wang, J. Yan, L. Duan, X. Li and H. Dong, The Effect of Liquid Nitriding on the Corrosion Resistance of AISI 304 Austenitic Stainless Steel in H_2S Environments, *Metall. Mater. Trans. A.*, 2018, **49**(12), p 6521–6532
22. P. Jacquet, J.B. Coudert and P. Lourdin, How Different Steel Grades React to a Salt Bath Nitrocarburizing and Post-Oxidation Process: Influence of Alloying Elements, *Surf. Coat. Technol.*, 2011, **205**(16), p 4064–4067
23. J.K.R. Sitek, M. Pisarek, H. Matysiak and K.J. Kurzydlowski, Corrosion Resistance of Inconel 718 Nickel Alloy After Pulsed Plasma Ion Nitriding at the frequency of 30 kHz, *Front. Appl. Plasm. Technol.*, 2011, **4**, p 6
24. K. Venkatesan, C. Subramanian, L.K. Green and K.N. Strafford, Influence of Chromium Content on Corrosion of Plasma-Nitrided Steels, *Corrosion*, 1997, **53**(7), p 507–515
25. Age-hardened Nickel-based Alloys for Oil and Gas Drilling and Production Equipment, 2015, API STD 6ACRA
26. H.S. Klapper and R.B. Rebak, Assessing the Pitting Corrosion Resistance of Oilfield Nickel Alloys at Elevated Temperatures by Electrochemical Methods, *Corrosion*, 2017, **73**(6), p 666–673
27. Standard Test Methods for Pitting and Crevice Corrosion Resistance of Stainless Steels and Related Alloys by Use of Ferric Chloride Solution, 2020, ASTM, G48
28. Standard Test Method for Electrochemical Critical Pitting Temperature Testing of Stainless Steels and Related Alloys, ASTM G150
29. Standard Test Method for Conducting Cyclic Potentiodynamic Polarization Measurements for Localized Corrosion Susceptibility of Iron-, Nickel-, or Cobalt-Based Alloys, ASTM G61 - 86, 2018
30. S.H. Elder, F.J. DiSalvo, L. Topor and A. Navrotsky, Thermodynamics of Ternary Nitride Formation by Ammonolysis: Application to Lithium Molybdenum Nitride (LiMoN2), Sodium Tungsten Nitride (Na3WN3), and Sodium Tungsten Oxide Nitride (Na3WO3N), *Chem. Mater.*, 1993, **5**(10), p 1545–1553
31. T. Bell and Y. Sun, Low-Temperature Plasma Nitriding and Carburising of Austenitic Stainless Steels, *Heat Treatment of metals*, 2002, **29**, p 8
32. J. Yan, J. Wang, Y. Lin, T. Gu, D. Zeng, R. Huang, X. Ji and H. Fan, Microstructure and Properties of SAE 2205 Stainless Steel After Salt Bath Nitrocarburizing at 450 °C, *J. Mater. Eng. Perform.*, 2014, **23**(4), p 1157–1164
33. M. Tsujikawa, N. Yamauchi, N. Ueda, T. Sone and Y. Hirose, Behavior of Carbon in Low Temperature Plasma Nitriding Layer of Austenitic Stainless Steel, *Surf. Coat. Technol.*, 2005, **193**(1), p 309–313
34. H.J. Spies, 6 - Corrosion behaviour of nitrided, nitrocarburised and carburised steels, *Thermochemical Surface Engineering of Steels Woodhead Publishing*. E.J. Mittemeijer, M.A.J. Somers Ed., Sawston, 2015
35. M.K. Bosslet, Salzbadnitrieren nach dem Tenifer-QPQ-Verfahren, Durferrit-Technische Mitteilung, Degussa AG, 2001, 2001
36. T. Borowski, K. Kulikowski, B. Adamczyk-Cieślak, K. Rożniatowski, M. Spychalski and M. Tarnowski, Influence of Nitrided and Nitrocarburised Layers on the Functional Properties of Nitrogen-Doped Soft Carbon-Based Coatings Deposited on 316L Steel Under DC Glow-Discharge Conditions, *Surf. Coat. Technol.*, 2020, **392**, p 125705
37. R. Sharghi-Moshtaghin, H. Kahn, Y. Ge, X. Gu, F.J. Martin, P.M. Natishan, R.J. Rayne, G.M. Michal, F. Ernst and A.H. Heuer, Low-Temperature Carburization of the Ni-base Superalloy IN718: Improvements in Surface Hardness and Crevice Corrosion Resistance, *Metall. and Mater. Trans. A.*, 2010, **41**(8), p 2022–2032
38. C.E. Foerster, F.C. Serbena, S.L.R. da Silva, C.M. Lepienski, C.J.M. de Siqueira and M. Ueda, Mechanical and Tribological Properties of AISI 304 Stainless Steel Nitrided by Glow Discharge Compared to Ion Implantation and Plasma Immersion Ion Implantation, *Nucl. Instrum. Methods Phys. Res. Sect. B Beam Interact. Mater. Atoms*, 2007, **257**(1), p 732–736

39. T. Borowski, Enhancing the Corrosion Resistance of Austenitic Steel Using Active Screen Plasma Nitriding and Nitrocarburising, *Materials*, 2021, **14**(12), p 3320
40. H.J. Grabke, The Role of Nitrogen in the Corrosion of Iron and Steels, *ISIJ Int.*, 1996, **36**(7), p 777–786
41. M. Marya, A Comparison of the Pitting and Crevice Corrosion of Directional Drilling Alloys With Oilfield Production Alloys, Corrosion-2020, p. NACE-14432, 2020
42. M.F. Yan and R.L. Liu, Influence of Process Time on Microstructure and Properties of 17–4PH Steel Plasma Nitrocarburized with Rare Earths Addition at Low Temperature, *Appl. Surf. Sci.*, 2010, **256**(20), p 6065–6071